



Facile Synthesis of ZnS/1T-2H MoS₂ nanocomposite for Boosted adsorption/photocatalytic degradation of methylene blue under visiblelight

Samira M. Abdel-Azim¹ · Mohammed M. Younus¹ · Abdelghaffar S. Dhmees¹ · Mehboobali Pannipara^{2,3} · S. Wageh^{4,5} · Ahmed A. Galhoum⁶

Received: 28 January 2022 / Accepted: 30 May 2022 / Published online: 7 July 2022
© The Author(s), under exclusive licence to Springer-Verlag GmbH Germany, part of Springer Nature 2022

Abstract

Facile solvothermal techniques were used to manufacture ZnS/1T-2H MoS₂ nanocomposite (ZMS) with outstanding adsorption-photocatalytic activity. The formed catalyst was characterized by different tools; XRD, HR-TEM, EDX, FTIR, Raman, N₂adsorption/desorption, Zeta potential, PL, and XPS. The analysis provided the formation on mixed phase of metallic 1T and 2H phases. ZMS has a high porosity and large specific surface area, and it has a high synergistic adsorption-photocatalytic degradation effect for MB, with a removal efficiency of ≈100% in 45 minutes under visible light irradiation. The extraordinary MB removal efficiency of ZMS was attributed not only to the high specific surface area (49.15 m²/g) and precious reactive sites generated by ZMS, but also to the formation of 1T and 2H phases if compared to pristine MoS₂ (MS). The best adsorption affinity was induced by the existance of 1T phase. The remarkably enhanced photocatalytic activity of ZMS nanocomposite can be ascribed to the 2D heterostructure which enhances the adsorption for pollutants, provides abundant reaction active sites, extends the photoresponse to visible light region.

Keywords Solvothermal-synthesis · 1T-MoS₂ · ZnS/1T-2H MoS₂ · Photocatalytic · Methylene blue

Highlights

- ZnS/1T-2H MoS₂ were synthesized by facile solvothermal method.
- The growth mechanism of ZnS/1T-2H MoS₂ based nanocomposite
- The effect of ZnS on the structure and morphology of ZnS/1T-2H MoS₂ has been investigated.
- The enhanced photocatalytic activity is attributed to synergetic interaction between ZnS/1T-2H MoS₂ and the separation of charge carriers.
- High concentrations of different scavengers inhibit the dye degradation process.
- Hydroxyl radical and superoxide radical anions contribution dominates in the degradation of MB dye.

Responsible Editor: Angeles Blanco

✉ Abdelghaffar S. Dhmees
Abdel_ghffar@yahoo.com

✉ Ahmed A. Galhoum
galhoum_nma@yahoo.com

¹ Egyptian Petroleum Research Institute, Nasr City, Cairo 11727, Egypt

² Research Center for Advanced Materials Science (RCAMS), King Khalid University, P.O. Box 9004, Abha 61413, Saudi Arabia

Introduction

Because many dyes have carcinogenic effects on humans and aquatic life, water pollution from synthetic is a developing environmental concern. Dyes are one of the most harmful pollutants from industrial effluents such as printing, textiles industries, and papermaking (Shen et al. 2020; Uddin et al. 2021; Waheed et al. 2021). Organic wastes will certainly be created during the application of organic dyes, which are

³ Department of Chemistry, College of Science, King Khalid University, P.O. Box 9004, Abha 61413, Saudi Arabia

⁴ Department of Physics, Faculty of Science, King Abdulaziz University, Jeddah 21589, Saudi Arabia

⁵ Physics and Engineering Mathematics Department, Faculty of Electronic Engineering, Menoufia University, Menouf 32952, Egypt

⁶ Nuclear Materials Authority, P.O. Box 530, El-Maadi, Cairo, Egypt

more difficult to breakdown due to their complex aromatic compounds and xenobiotic characteristics (Liao et al. 2019; Shen et al. 2020). To eliminatedyes from industrial wastewater numerous technologies such as coagulation, advanced oxidation, membrane separation, and adsorption have been utilized (Uddin et al. 2021; Waheed et al. 2021).

Adsorption is a well-developed technology for removing dyes from wastewater since it is a simple process with a lower cost than other methods (Galhoum 2019; Waheed et al. 2021; Zheng et al. 2019). However, the process of dye removal from industrial wastewater using conventional adsorbents is not sufficiently efficient (Issaabadi et al. 2017; Uddin et al. 2021; Waheed et al. 2021). But, one of the most promising methods is photocatalysis as an efficient, simple method, and no need for assisting agents to eliminate the organic pollutants from wastewater. As a result, developing ecologically acceptable, sustainable, simple, quick, easy-to-control, and energy-efficient ways for preparing adequate catalytic activity remains a challenge. As their fundamental importance applications for solving energy and pollution problems, semiconductor photocatalysts have attracted a subject of extensive interest (Cheng et al. 2017; Liao et al. 2019; Zhang et al. 2020a).

Henceforward, adsorption enhanced by a photocatalytic technology has now been investigated as a novel and consistent method for the cleanup of persistent contaminants. Pollutants adsorption by the photocatalyst is regarded a necessity and pre-requisted, under visible region (Ebrahimi et al. 2021; Gao et al. 2021; Pathania et al. 2021).

Because numerous photocatalysts have been employed to degrade organic pollutants, including TiO_2 (Mahmoodi et al. 2006), $\text{SiO}_2/\text{CeO}_2$ (Dhmees et al. 2019), Bi_2WO_6 (He et al. 2021), ZnS-ZnO/MCM-41 (Amdeha et al. 2021), and MoS_2 (Cheng et al. 2017). 2D Transition Metal Dichalcogenides (TMDs) such as MoS_2 , WS_2 , and others has ignited interest in the fields of energy harvesting, storage, and water treatment.

Photocatalytic method produce highly reactive oxygen species (Gao et al. 2021). These radicals have the ability to degrade harmful compounds into innocuous products. This method is safe, applicable, and has a higher visible area absorption with excellent photochemical stability (Hayati et al. 2021; Kumar et al. 2021; Pathania et al. 2021). Molybdenum disulfide (MoS_2) is a typical photocatalyst in photocatalytic oxidation technologies that may successfully breakdown numerous contaminants and toxins (Cheng et al. 2017; Cheng et al. 2022).

Layered MoS_2 is an inorganic equivalent of graphene, with a sandwiched structure created by the weak Vander Waals' force in the S-Mo-S form. MoS_2 is a widely used material in Li-ion batteries (Liu et al. 2020a), supercapacitors (El Sharkawy et al. 2020; Elkholy et al. 2019), waste water purification (Wang et al. 2020), catalysis (Cheng

et al. 2022), sensors (Ding et al. 2021) and other uses, due to its low toxicity, low cost, thermal stability, and oxidising properties. Despite having enormous active sites and a large surface area, layered MoS_2 provides excellent photocatalytic reactions. However, due to the fast recombination of photoexcited electrons and holes, it lags behind in industrial applications (Yu et al. 2019). As a result, it is suggested that hetero-structures be created by mixing two different semiconducting materials in order to accomplish effective photo-excited electron and hole separation (Yu et al. 2019). The hexagonal 2H phase of natural MoS_2 is made up of a sandwich structure of S–Mo–S. (semiconductor phase). There is another metastable octahedral 1T (metallic) phase MoS_2 , which has better catalytic activity than 2H- MoS_2 (Chang et al. 2016) Pure 1T- MoS_2 , on the other hand, have two fatal defects: a metastable state and need extremely harsh synthesis conditions, both of which severely limit its use (Geng et al. 2017; Zhang et al. 2020c). To overcome these problems, current researchers have discovered that by introducing 1T- MoS_2 into 2H- MoS_2 , the number of catalytically active sites in MoS_2 may be enhanced effectively while retaining stability. Zinc sulphide (ZnS) is a well-known semiconductor photocatalyst with a broad band gap energy (3.2–4.4 eV) that may be utilised to segregate photo-induced electrons and holes in MoS_2 .

Thus, in our present study, the hydrothermal reduction has been preferred due to its high purity of the material, low-temperature reaction, and large production rate (Krishnan et al. 2019). Due to there have been few studies on nanocomposite of ZnS/MoS_2 . Herein, this work focuses on the ZnS/1T-2HMoS_2 nanocomposite synthesis as a heterogeneous photocatalyst via a simple solvothermal three components one-pot reaction. The catalytic activity of the as-product ZnS/1T-2HMoS_2 nanocomposite (ZMS) has been compared and evaluated to those of pristine MoS_2 (MS) (rather than ZnS (ZS)) for the methylene blue (MB) degradation: which can be reused for five photocatalytic reaction cycles. The physicochemical specifications of these prepared catalysts were extensively examined by XRD, EDX, BET, XPS, Raman, HR-TEM, FTIR, PL, UV-visible, TOC, and Zeta-potential.

Experimental

Materials and analysis

Sodium molybdate ($\text{Na}_2\text{MoO}_4 \cdot 2\text{H}_2\text{O}$, 99.9%) and zinc acetate ($(\text{CH}_3\text{COO})_2\text{Zn} \cdot 2\text{H}_2\text{O}$, 98.5%) were purchased from BDH Chemical Ltd. Ethanol (99.0%) and ethylene glycol were provided by Fisher Chemical. Thiocarbamide ($(\text{NH}_2)_2\text{CS}$, 99.0%) was supplied by Merck. All analytical

grade compounds were used as obtained. Methylene blue (MB) (A.R grade, FineChem., India) was measured spectrophotometrically (using a HITACHI U-4100 UV–Vis spectrometer) at λ_{max} : 664 nm (Sabarinathan et al. 2017).

Preparation of ZnS/MoS₂

MoS₂ and ZnS/MoS₂ catalysts were synthesized applying the following method. Initially, Ultrasonication was used to dissolve Na₂MoO₄·2H₂O (1 mmol) and (CH₃COO)₂ Zn (1 mmol) in C₂H₅OH (40 mL), then (NH₂)₂CS (4 mmol) was added under continuous sonication for another 30 minutes, at room temperature (298 K). After that, the homogeneous clear mixture was put into a Teflon-lined stainless autoclave (100 mL), which was kept at 180°C in an oven for 12 hours. Afterward, centrifugation was used to collect the resulting black powder, which was then extensively washed with water and ethanol. The ZnS/MoS₂ was vacuum dried at 60°C for 12 hours. While the pristine MoS₂ was prepared under the same conditions and procedures but in absence of zinc salt.

Characterization

Using Philip's PW1390 X-ray diffractometer, Cu K α (λ : 1.544) to investigate the crystal structure of prepared catalysts. The surface charge and stability of prepared catalysts: Zeta-potential was performed using Dynamic light scattering (DLS, UK). Quanta Chrome Nova 3200 analyzer was used to evaluate Textural properties using N₂-adsorption/desorption isotherms at 77 K. A Nexus-870 FTIR spectrometer was used to measure the Fourier transform infrared (FTIR) analyses, Nicolet, USA. The surface morphology of the catalyst was investigated by high-resolution transmission electron microscopy (HR-TEM Model JEM-200CX, JEOL, Japan). The elemental composition and distribution mapping was measured by energy-dispersive X-ray spectroscopy (EDS). Using SENTERRA Dispersive Raman Microscope (Bruker, Billerica, USA), Laser Raman analysis was conducted at room temperature. The UV–vis diffuse reflectance spectroscopy (DRS) study of the produced photocatalysts was performed using a JASCO (Japan). The photoluminescence characteristics were evaluated using a spectrofluorometer (JASCO FP-6500, Jasco, Japan). X-ray photoelectron spectroscopy (XPS) was used to identify the catalyst structure (Thermo Fisher Scientific, Waltham, MA, USA). The total organic carbon (TOC) analyzer was used to evaluate the degree of mineralization (TOC/TN Analyzer multi N/C Series-Analytik Jena, German).

Photocatalytic studies

The photocatalytic activity of both prepared ZMS compared to pristine MS was evaluated for degradation of methylene

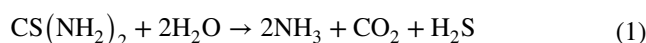
blue (MB) under visible light. A tungsten halogen lamp (400–800 nm) was a visible light irradiation source (power 50W). The sample and the source of irradiation are separated by about 50 cm. Typically, catalyst (20 mg) was immersed in MB solution (20 mL, C₀: 10 mg MB L⁻¹). Before irradiation, to reach the sorption/desorption equilibrium, the solution was sonicated for 60 minutes in the dark with magnetically swirled. At predetermined intervals of time, the sample solution (5 mL) was collected and then centrifuged. The MB concentration was measured spectrophotometrically (Sabarinathan et al. 2017). The MB's photodegradation percentage was calculated using a mass balance equation: $D(\%) = ((C_0 - C_t) / C_0) \times 100$, where C₀ and C_t (mg/L) are the concentration of MB at time 0 and t, respectively; and t is the period between sample intervals.

Results and discussion

The growth mechanism of ZnS/1T-MoS₂ based nanocomposite

One of the most essential tools for enhanced materials processing of mono-dispersed nanoparticles of diverse metal oxides is the hydrothermal approach (Krishnan et al. 2019; Vattikuti et al. 2016). Sodium molybdate (Na₂MoO₄·2H₂O) used Na₂MoO₄·H₂O used as a source of molybdenum. Wang et al. (Wang et al. 2010), suggested that the reaction involves a complex process, which contains three steps: (a) the hydrolysis of CS(NH₂)₂ to form H₂S; (b) the reduction of Mo(VI) to lower valent produce Mo(IV); (c) the formation of MoS₂ nanosheets. The synthesis of MoS₂ can be described as a reaction process as follows:

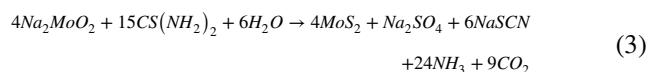
The hydrolysis of thiourea CS(NH₂)₂ to form H₂S (acts as a reductant):



The solubility equilibrium of Na₂MoO₄·2H₂O in aqueous solutions can be described as follows:



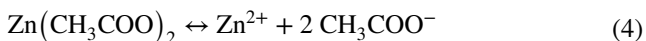
When sodium molybdate reacted with thiourea, Mo^(VI) is reduced to lower valent Mo^(IV) followed by further sulfurized to produce a black precipitates of MoS₂ (pristine MoS₂):



There are few publications on the role of zinc acetate and thiourea (complexes) in the synthesis of ZnS by the sol-gel method (Ashoka et al. 2009; Auer et al. 2000) here was no visible reaction when zinc acetate and thiourea were

combined together, and the solution remained clear. The reaction appears to be reliant on externally provided thermal energy. The solution generated a complex $[\text{ZnCS}(\text{NH})_2]$ when it was refluxed at 90°C . Due to heat energy, the obtained complex continually interacted with water in the solution and converted into ZnS, CO_2 , and NH_3 .

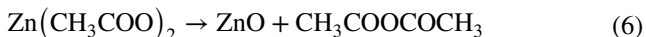
The reaction process could be expressed as follows:



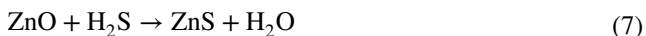
Then further H_2S (obtained from the thiourea hydrolysis (Eq. 1)) reacts with Zn^{2+} to yield ZnS nanoparticles.



Ashoka et al. stated that zinc acetate was used as a precursor, can undergo decomposition in water-ethylene glycol mixture, and forms ZnO nuclei at lower temperature region below 100°C without forming any intermediates (Ashoka et al. 2009). The possible reaction for the formation of ZnO (this suggested agreed with the XPS results) is as follows:



The reaction of ZnO with $\text{H}_2\text{S}_{(\text{g})}$ (i.e. sulfidation reaction) is as follows:



where ZnO is used to scavenge $\text{H}_2\text{S}_{(\text{g})}$ impurities in the natural gas (Auer et al. 2000).

The mechanisms to produce these reactions

At a hydrothermal temperature at 180°C , the MoS_2 nuclei self-assembled to form the laminated nanostructures along with a preferred axis orientation. There are abundant sulfur vacancies distributed on the edge of the MoS_2 layered structure. The more stable cubic form of ZnS exists in two primary crystalline forms (coordination geometry at Zn and S is tetrahedral (zinc blende) and hexagonal (wurtzite)), and this dualism is an example of polymorphism (coordination geometry at Zn and S is tetrahedral (zinc blende) and hexagonal (wurtzite)). ZnS exists in two polymorphs at ambient temperatures: cubic zincblende and hexagonal wurtzite.

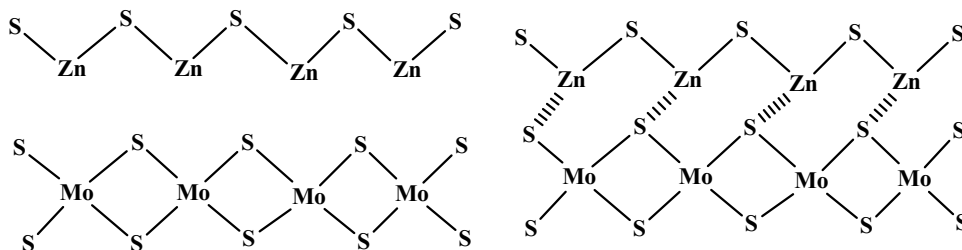
Under typical conditions, the latter is metastable and easily converts to the cubic form (Zhao et al. 2015). MoS_2 generated on the surface of ZnS, the electrons transfer from Zn to Mo through the S atom and formed the Zn-S-Mo structure (Fig. 1). These results match with the results obtained from the XPS results. The reaction between ZnS and the MoS_2 nanosheet molecules in the nanocomposite matrix doesn't form any coordination bonds but are stabilized by weak columbic or Van der Waal's interactions. Such interactions between the nanocomposite's ingredients can improve current features while also introducing exciting new characteristics. The higher negative zeta-potential of MoS_2 (-36 mV), compared with ZnS/ MoS_2 (-22 mV), as MoS_2 possess many S-atoms with large electronegativity which can attract Zn which has positive charges.

Materials Characterization

XRD analysis

XRD pattern was applied to emphasize the as-synthesized ZS, MS and ZMS nanocomposite formation and evaluate its crystalline phase (Fig. S1). A typical crystalline peaks appeared at 2θ angle: 28.49° , 47.51° and 56.33° , respectively to (111), (220) and (311) cubic planes of ZnS according to (JCPDS 65-0309), with a very weak shoulder at 34.2° for (200) (Lydia Caroline and Vasudevan 2009, Vattikuti et al. 2016). While the pure MoS_2 pattern is primarily due to the amorphous and nanocrystalline MS, these findings are consistent with the obtained amorphous MoS_2 nanoflakes (Liu et al. 2020b). The ZMS XRD pattern is quite consistent with the pure cubic phase of ZnS nanoparticles (Wahab et al. 2009). No distinctive MoS_2 diffraction peaks were identified in ZMS, but the (111) diffraction peak of ZnS at 28.49° was shifted to lower 2θ at 28.33° . This shift may be related to the difference between Mo and Zn in atomic radius (Hu et al. 2018). The main cause for the absence of MoS_2 characteristic peak related to that reaction temperature (180°C) is not sufficient to give good peaks of crystallinity (Hou et al. 2020). The crystallinity of MoS_2 nanosheets was reported to depend on the sulfur precursors, amount, preparation method,

Fig. 1 Schematic view of the structure of the Zn-S-Mo phase



temperature, and reaction time (Gopalakrishnan et al. 2020; Hou et al. 2020; Liu et al. 2020b); high temperatures and long reaction time usually contribute to increasing the crystallinity (Hou et al. 2020).

EDX analysis

Figure S2 displays EDX measurements for ZS, MS, and ZMS: exhibited the existence of all the elements Zn, Mo, and S signals constitutive of the corematerials. In the EDX spectra: the specific peak of the Zn element was characterized by $L_{\alpha 1}$ and $L_{\beta 2}$, which their peaks at 8.639, 9.572, and 1.012 keV, respectively. The characteristic $K_{\alpha 1}$ and $K_{\beta 1}$ peaks for S were exhibited at 2.307 and 2.464 keV, near 2.39 keV reveals the L_{α} of Mo (Soltani et al. 2012).

Textural characteristics

The textural properties of the two MS and ZMS catalysts (specific surface area (SSA_{BET}), pore volume, and pore diameter) have been analyzed by N_2 ads/desorption isotherms (Fig. S3)). According to the IUPAC classification, ZMS pertain to a type-IV curve with an H_3 hysteresis loop, suggesting a mesopores catalyst. The introduction of Zn into MoS_2 layers improved and enhanced the SSA_{BET} of pristine MS from $16.23 \text{ m}^2 \cdot \text{g}^{-1}$ to $49.31 \text{ m}^2 \cdot \text{g}^{-1}$ in ZMS (i.e. 3.1 times). These trends are consistent with the differences observed in the average pore size: the average pore size increases from $\sim 3.52 \text{ nm}$ for ZMS to $\sim 4.40 \text{ nm}$ for MS resulting in ZMS nanocomposite larger surface area. Also,

the same observation for the pore volumes were: $0.034 \text{ (cm}^3/\text{g)}$ and $0.025 \text{ cm}^3/\text{g}$ for MS and ZMS, respectively.

HR-TEM

Figure 2 shows the HR-TEM images of the prepared ZMS nanocomposite. The morphology of nanosheets as exfoliated has a typical layered structural morphology with several edge nanolayers. The ZnS nanoparticles have appeared as spherical dense dots (surrounded by bright layers representing the MoS_2 nanosheets, which could be due to the difference of electron-absorbing differences between both metal–sulfide phases. The TEM-images reveal nanosheets with several 100 nm in size with irregular shapes. The thin nanolayers with an interlayer spacing of 0.68 nm were assigned to the MS as illustrated in Fig. 2B: where MoS_2 nanolayers (red areas) were occasionally apparent. The mapping characterization of the layers structure using energy-dispersive X-ray spectroscopy (EDS) (Fig. 2(C–F)). The mapping analysis demonstrates the good homogenous distribution for elements Zn, Mo, and S.

XPS

The chemical composition and surface oxidation state of ZMS were confirmed by XPS analysis (Fig. 3) which agrees with the EDS results. The high-resolution spectra for Mo 3d can be separated into five peaks: the peak at roughly 226.1 eV is assigned to the S 2s of MoS_2 , while the peaks at 229.8 and 235.3 eV are attributed to the Mo $3d_{5/2}$ and Mo $3d_{3/2}$ of Mo^{6+} , respectively (Zhao et al.

Fig. 2 A) TEM image, B) HRTEM image of ZMS, and C–F) EDX-mapping of the ZMS sample (SEM micrograph; Zn, Mo, and S distribution cartographies)

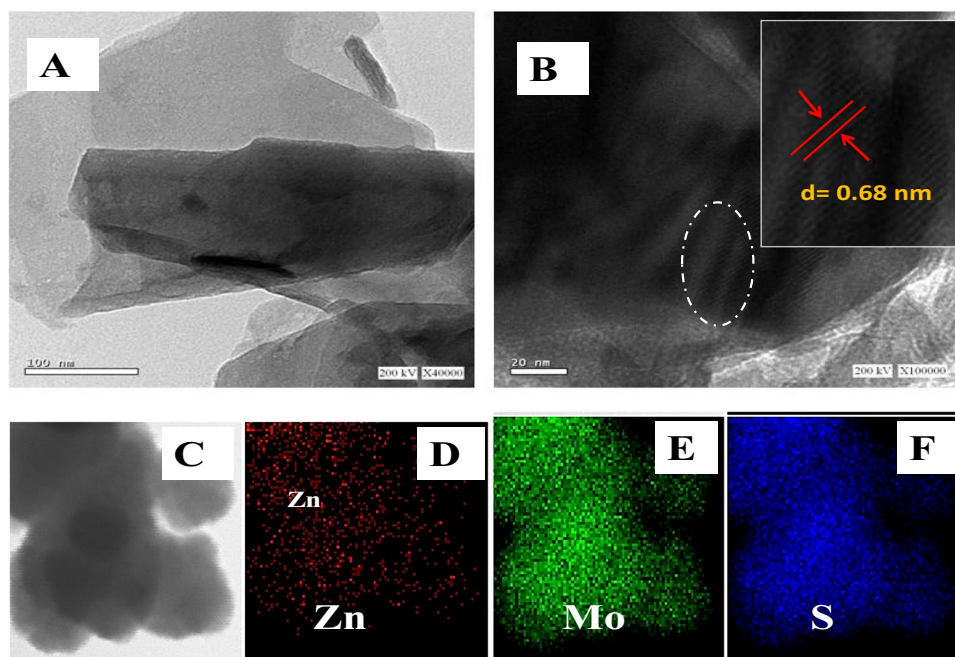
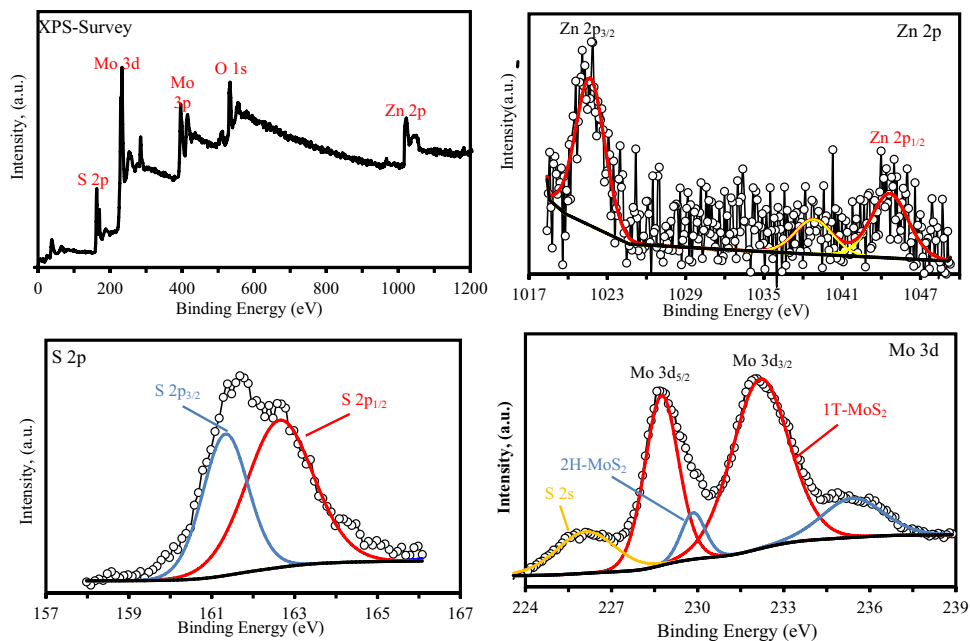


Fig. 3 XPS spectra of Mo 3d, Zn 2p, O 1s, and S 2p in the as-prepared ZMS nanocomposite



2014). The Mo 3d_{5/2} peak indicates that Mo is found as a hexavalent oxide (Mo⁶⁺). The Mo 3d_{5/2} and Mo 3d_{3/2} of Mo⁴⁺ in MoS₂ have two more peaks at 228.8 and 231.9 eV, respectively (Harish et al. 2019). The peaks of Mo 3d: 228.8 eV and 231.9 eV (3d_{5/2} and 3d_{3/2}) are said to correspond to 1T-MoS₂ phase (metallic), while 229.8 eV and 235.3 eV (3d_{5/2} and 3d_{3/2}) are reported to correspond to 2H-MoS₂ phase (Zhao et al. 2014), indicated a mixed phases of 1T-MoS₂ and 2H-MoS₂ (Zhao et al. 2014). The spectra of Zn 2p splits the two emission peaks of Zn 2p_{3/2} and Zn 2p_{1/2} at: 1022.8 eV and 1044.9 eV, respectively, and this result is consistent with the binding energy of Zn²⁺ in ZnS (Harish et al. 2019). The values are 1.0 eV higher than pure ZnS owing to the strong interaction between MoS₂ and ZnS (wurtzite-type) via the sharing of metal sulphide bonds between Mo and Zn (Rao Akshatha et al. 2020). The asymmetric S 2p peak was deconvoluted into two subpeaks corresponding to S 2p_{3/2} and S 2p_{1/2} are observed at 162.3 eV and 163.5 eV, respectively, indicating the S²⁻ presence (Rao Akshatha et al. 2020; Zhang et al. 2020a). However, the intensity ratio of the spin-orbit splitting S 2p_{3/2} and S 2p_{1/2} was about 1:1 (is not 2:1); this can be attributed to the increased bonding states of sulfur-related surface defects in Mo-S-Zn (Mao et al. 2015; Rao Akshatha et al. 2020). These results correspond to ZnS, MoS₂, and Zn-S-Mo respectively. The S 2p_{3/2} peak was attributed to the typical metal-S bond, while the S 2p_{1/2} peak was corresponding to the sulfur with low coordination, which is generally related to sulfur defects (Gao et al. 2015; Zheng et al. 2019). Surprisingly, the observation of two signals at 284 eV and 533 eV, respectively, that

represents C 1s peak (C=O /and C-OH groups) and O 1s signal together (Tolba et al. 2017). For the O 1s signal consistently with the ZnS formation mechanism above. This confirms the presence of traces of carboxylic groups from Zn-acetate salt could be due to the insufficient washing or incomplete reaction, or the CO₂ gas adsorption as in FTIR analysis (not shown).

Raman

As shown in Fig. S4, the Raman spectrum of ZS shows mainly the first-order modes at ~265.5 cm⁻¹ and ~354.0 cm⁻¹ corresponding to the transverse optical (TO) and longitudinal optical (LO) phonon (Cheng et al. 2009, Lin and Ho 2017). In addition, other Raman peaks at 145 cm⁻¹, 175 cm⁻¹, 386 cm⁻¹, and 440 cm⁻¹ are also (Zamiri et al. 2014). On the other hands, The existence of 2H- and 1T-phases of MS and ZMS were confirmed by Raman measurements (Fig. S4). The 2H-phase has two notable bands at 383 cm⁻¹ (E_{12g}¹) and 409 cm⁻¹ (A_{1g}¹). However, the pristine MoS₂ give a low peak at 383 cm⁻¹ (E_{12g}¹) which come from the atom's motion along the x-axis, and ZMS give also a small band at 412 cm⁻¹ (A_{1g}¹) that attribute to the S atoms' motions along the Z-direction (Zhang et al. 2020b). Typical and high-intensity peaks at 146 (J₁), 226 (J₂), and 333 cm⁻¹ (J₃) confirm the formation of high percentage in metallic phase of 1T-MoS₂ nanosheets (Zhang et al. 2020b; Zhao et al. 2014). The significant change (peak width, intensity, and shifted) in ZMS nanocomposite and the intensity peak of the ZMS at 333 cm⁻¹ is much higher than that of MS, confirm the good effect of ZS on MS phase to stable 1T phase.

Zeta Potential

Figure S5 shows the zeta potential values for MS and ZMS were measured as a function of pH. The ζ -potential values at pH 6.0 are -16 mV for MS and -5 mV for ZMS and its value increase with increasing the pH. The surface is negatively charged over the pH of zero point charge (pH_{ZPC}): 4.15 and 4.95 for MS and ZMS, respectively. The negative charge of MS and ZMS provides high dispersion and improves the capture of cationic dyes (MB⁺).

Optical absorption

The band gap energy of semiconductors can be calculated using the equation $\alpha h\nu = A(h\nu - E_g)^{1/2}$, which is based on the link between absorbance and photon energy, where α and $h\nu$ represent the absorption coefficient, and incoming photon energy, respectively, A is a constant, and E_g represents the material's band gap. Thus, for ZMS the band gap was calculated to be 2.75 (as shown in Fig. S6), while for ZS and MS were 3.6 and 1.86, respectively (Li et al. 2018; Lin et al. 2015; Zhang et al. 2020a). It is clear that MoS₂ modified with ZnS is more favorable in terms of improving light absorption, lowering the band gap, and changing the electrical structure of MS (Lin et al. 2019).

Photoluminescence (PL)

The photocatalytic efficiency of a catalyst is mainly controlled by the separation and migration of the photo-generated charge carriers, because if the electron-hole pairs recombine during the photocatalytic process a significant amount of photonic energy is lost. The recombination of a photo-generated hole with an electron occupying the oxygen vacancy causes the emission wavelength to be precisely connected to the energy band-gap. Therefore, it is vital to suppress the recombination of charge carriers to increase the activity of the catalyst. Thus, the PL spectra have been used to investigate carrier trapping and recombination of charge carriers. Figure S7 shows PL obtained for the pristine MS and ZMS catalysts, in the range from 250–550 nm at a 280 nm excitation wavelength. Because the band gap, doping, and structure of the material all influence the PL spectra, MS have a variety of PL activity (Nezamzadeh-Ejhi and Banan 2011). Both catalysts showed one broad luminescence/emission peak (Fig. S7), a well-defined peak was noticed in the spectrum at λ_{\max} : 402 nm which can be attributed to the radiation recombination of free charge carriers for the inter-band (CB-VB); that emits light with the same or slightly higher energy as the band gap of catalysts. Moreover, with additional weak peaks/shoulders at λ : 533 nm, 488 nm, 460 nm, 438 nm, 423 nm, 350 nm, 288 nm, and 273 nm. The position of the major peak at λ_{\max} : 402 nm

in the MS, is not affected in ZMS, but its intensity is significantly reduced by doping with ZS: as the metal sulfides can function as agents to capture photo-produced electrons (Vattikuti et al. 2016). Hu et al. reported that the PL intensity of ZMS is substantially weaker and lower than pure ZS and pure MS (Hu et al. 2018). The lower PL intensity indicates that the recombination of holes (h⁺) and electrons (e⁻) is slower, indicating strong photocatalytic activity, and the catalytic activity is then increased (Hu et al. 2018; Morshedy et al. 2021).

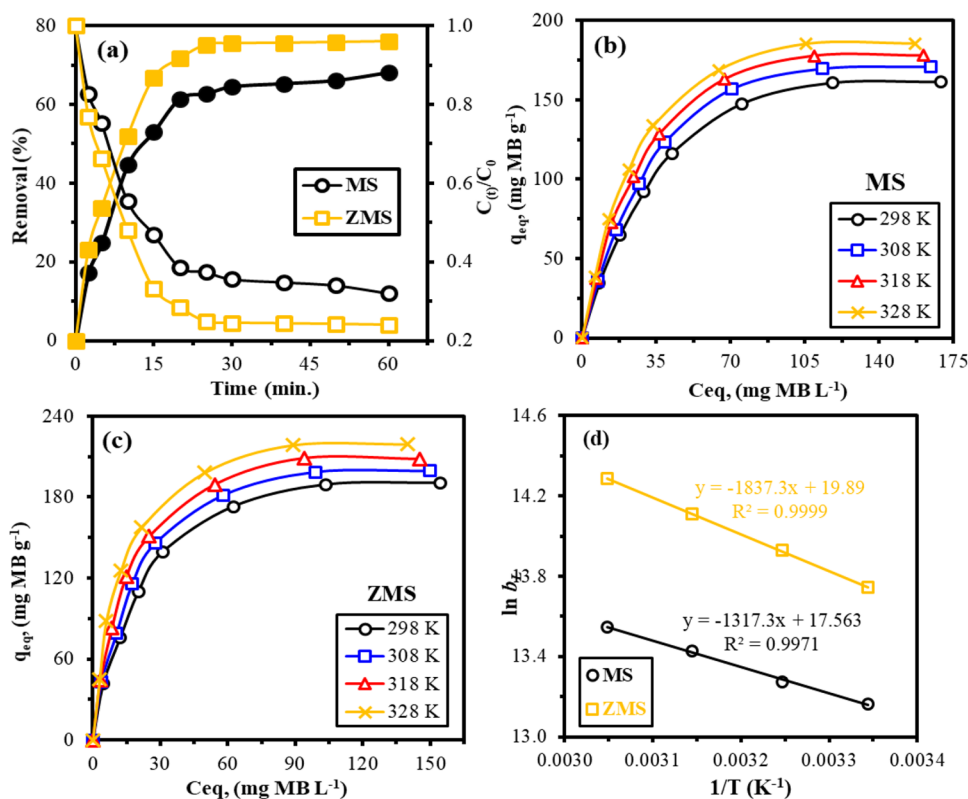
Photocatalytic activity

Sorption equilibration-time

The degradation of MB dye effluents is a critical problem that has to be investigated (Azad et al. 2011). So, the catalytic activity of MS and ZMS nanocomposite in MB degradation is studied using the visible light lamp. The MB solutions were agitated for 60 minutes before photocatalytic degradation to achieve ad-/de-sorption equilibrium between MB⁺ dye and photocatalyst. In dark area: MB⁺ ions adsorption was compared for both catalysts (for the first 60 min before irradiation) (Fig. 4). Obviously, ZMS shows higher removal efficiency compared to pristine MS, whatever the time. Both curves, regardless of the catalyst type, exhibit comparable directions (Fig. 4). Within the first 10 min, a very fast initial sorption capacity accounts for around 69.2% of total capacities. While, the removal efficiencies were about 44.6 and 52.0% for MS, and ZMS, respectively, the removal efficiency (vs. time) in the dark area before irradiation increased almost linearly (matching to a physisorption process) and then gradually decreased as the time of reaction increased (10 to 25 minutes): after that, a chemical reaction involving charge neutralization and chelation is carried out until equilibrium is reached (Galhoum 2019). The negatively charged layer attracts the MB⁺ to MS and ZMS surface to initiate the photocatalytic reaction (Azad et al. 2011). After that, the sorption rate of MB⁺ ions approached saturation and nearly zero due to the sorption equilibrium reached within 25/30 min. for MS and ZMS, respectively. Extending the contact period up to 180 minutes and 24 hours, according to preliminary investigations, has no significant effect on removal performance. The change in the MB removal efficiencies rate depends mainly on the accessible sorption sites. Furthermore, as sorption duration increases, sorption rate reduces due to a decrease in the concentration gradient and the contribution of the intraparticle diffusion resistance mechanism

Moreover, last step is controlled by resistance to intraparticle diffusion through internal micropores. The high adsorption affinity of ZMS almost related to highly surface area of as-prepared ZMS catalyst which valued nearly the three

Fig. 4 MB⁺sorption uptake kinetics before irradiation using MS and ZMS sorbents—relative residual concentration versus contact time (at C_0 : 50 mg MB L⁻¹ and 25 °C) (a), Sorption isotherms (b & c), and Thermo-dynamics—Van't Hoff plots of $\ln b_1$ vs $1/T$ (d). (pH₀: 6.8, SD: 0.5 g L⁻¹, C_0 : 25.4–249.8 mg MB L⁻¹, T: 25–55 °C, Time: 60 min.)



times more than of MS. As a result, 30 minutes is enough time to reach equilibrium (Cheung et al. 2007). The kinetics key equations for modelling are shown in Table S1 (see Supporting Information Section) (Hu et al. 2021). Complex models exist for systems where intraparticle diffusion resistance is a controlling factor. Weber-Morris plots (Fig. S8), which show diverse diffusion behaviors, corroborate these trends. External surface adsorption is represented by the binding of MB⁺ ions on the active sites at the surface of the particles in the first part with a steep slope. The second part involved progressive diffusion in micro- and mesopores, where intraparticle diffusion was rate-controlled and slowed due to the low dye content in solution (Galhoum 2019). These multi-linear plots are the result of the MB⁺ diffusion performance. It's worth noting that the values of intraparticle diffusion rate constants ($K_{id,1}$ & $K_{id,2}$) were higher, with the sequence ZMS > MS, implying faster sorption processes for ZMS. For diverse sorbents, the third rate constants ($K_{id,3}$) values were nearly close to zero, implying that the equilibrium state had been reached (Cheung et al. 2007; Galhoum 2019; Hu et al. 2021).

Furthermore, the pseudo-first-order rate equation (PFORE) and pseudo-second-order rate equation (PSORE) have been used to simulate uptake kinetics (Cheung et al. 2007; Hu et al. 2021). PSORE is based on the assumption that adsorption follows the chemisorptions mechanism and predicts behaviour over the entire concentration range.

While PFORE assumes that the rate of change of solute uptake with time is directly proportional to the difference in saturation concentration and the amount of solid uptake with time. As well as, PFORE assumes that the rate of change of solute uptake with time is directly proportional to the difference in saturation concentration and the amount of solid uptake with time (Cheung et al. 2007, Galhoum 2019, Hu et al. 2021, Tien 1994). The aforementioned kinetics models were used to fit the experimental data, and their particular parameters (along with their distinct correlation coefficients, R^2) are displayed in Table S2. Figure S9 demonstrate that the PSORE fitted experimental data better than the other models (including PFORE). The comparison of the equilibrium sorption capacities (q_{eq}) shows that the PSORE allows approaching closer to the experimental value than the PFORE: the Δq_{eq} overestimates ranges between (9.8–16.5%) for PFORE, while for the PSORE by (9.9–15.8%). Additionally, the correlation coefficient for the PSORE ($R^2 \approx 0.99$) was higher than in the case of the PFORE ($R^2 < 0.99$).

Moreover, the comparison of the apparent rate coefficients for PSORE (k_2): where k_2 values were 30.0×10^{-4} mg g⁻¹ min⁻¹ for ZMS and 23.5×10^{-4} mg g⁻¹ min⁻¹ for MS; confirming the faster sorption for ZMS. Based on the obtained k_2 , the half-adsorption time ($t_{0.5}$: defined as the time required to reach half the amount of the maximum sorption capacity by the ion-exchange resins) was determined. The $t_{0.5}$ could be used as a measure of the adsorption rate, as described

by Eqn ($t_{0.5} = 1/k_2 \cdot q_2$) (Doğan et al. 2007). In addition, the $t_{0.5}$ for MS (5.7 min) are significantly higher by 1.39 times than for ZMS (4.1 min). This indicates that the MB⁺ sorption is more favorable by ZMS, this finding agrees with the experimental results.

Sorption isotherms

As a function of initial MB concentration (25.4 - 249.8 mg MB L⁻¹) solutions were investigated at neutral pH₀ 5.5 and different temperatures (298 - 328 K) to evaluate the sorbents capacities. As a forceful force, it overcomes the resistance of mass transfer between the solution and solid phases in the sorption process (Ibrahim et al. 2021; Neiber et al. 2022; Rashad et al. 2021). Figure 4 compares MB⁺ sorption isotherms; with increasing the C₀ and C_{eq}, the sorption capacity progressively increases as all accessible sites on the sorbent surfaces were occupied. The equilibrium concentration-sorption diagram of the isotherm, shown in Fig. 4, is characterised by; with an ever-increasing the initial, and equilibrium concentration, a gradual increase in sorption capacity, followed by sorbent saturation at maximum experimental sorption capacity ~191.5 and 161.1 mg MB L⁻¹, for ZMS and MS, respectively at 298 K. The plateau revealed that the sorbent's most active sites reacted with MB. This illustrates the superiority of ZMS sorption capacity over MS: systematically with the equilibration time findings. This sequence can be explained by the multi-functionality and the higher active site density for ZMS than MS sorbent. The sorption capacities order is consistently with the properties of SSA_{BET} of the sorbents (ZMS > MS); that influences the accessibility to reactive sites.

The linear forms of the Langmuir and Freundlich equations were used to investigate the sorption isotherms (Liu et al. 2019; Tien 1994). The key equations used to model the isotherm profiles are listed in Table S1. The fitting of data profiles with the Langmuir and Freundlich equations is compared in Fig. S10. Table S3 lists the key parameters of these models. The comparison of determination coefficients (R²) for the Langmuir generally gives slightly higher coefficients (R² > 0.99) compared to Freundlich (R² < 0.96). In addition, the sorption capacities were consistent with experimental results and were systematically overestimated using the Langmuir model (Δq_{eq} : 8.9-14.9%, for ZMS, and 17.2-24.2% for MS), while where underestimated for the Freundlich (Δq_{eq} : 84.0-88.4% and 90.5-92.8% for ZMS and MS, respectively).

Table S3 illustrates the b_L values (the Langmuir constant related to the sorption energy) were nearly duplicated for ZMS compared to MS sorbent. Moreover, the b_L values increased, for ZMS (from 523.92-to-903.23 L mg⁻¹), and for MS (from 293.60-to-430.71 L mg⁻¹): with increasing the temperature from 298 to 328 K, consistently with previous observations of q_m . This indicates the sorption is

more favorable at higher temperature. The greater the b_L value, the higher the sorption energy, and the stronger the sorbent-sorbate affinity (Neiber et al. 2022, Rashad et al. 2021) The generated curve is close to experimental points, demonstrating the Langmuir equation's ability to fit the sorption isotherm. The saturation plateau corresponds to the asymptotic trend associated with the Langmuir equation, whereas the Freundlich equation is a power-like function, as expected based on the structure of sorption isotherms (Neiber et al. 2022, Rashad et al. 2021). This demonstrates that metal sorption occurs by monolayer uniform sorption, which involves a finite number of identical sites spread across the sorbent surface.

Another model is the Temkin isotherm supposes that sorption free energy is proportional to surface coverage (Liu et al. 2019, Tien 1994). The Temkin model constants are reported in Table S3 and Fig. S10. The constant A_T represents the sorbent initial sorption heat: the higher the A_T , the greater the sorption heat, and the higher the sorbent's affinity for the sorbate (Liu et al. 2019). The A_T values increased from 46.11 to 47.25 L/g and 45.59 to 48.368 L/mg for ZMS, and MS, respectively, while the energetic parameter (A_T) decreased as follow: ZMS (0.539-to-1.063 J/mol) > MS (0.265-to-0.368 J/mol); with increasing the temperature from 298 K to 328 K, as previously observed (such as comparison of b_L and q_m in the Langmuir model (Liu et al. 2019).

Based on the Langmuir isotherms, the thermodynamics might be examined. Thermodynamic parameters are calculated by the van't Hoff equation (Liu et al. 2019; Neiber et al. 2022; Tien 1994).

$$\ln b_L = -\frac{\Delta H^0}{R} \times \frac{1}{T} + \frac{\Delta S^0}{R} \quad (8a)$$

$$\Delta G^0 = \Delta H^0 - T\Delta S^0 \quad (8b)$$

where, the universal gas constant is R (8.314 J/mol.K), T (K) indicates absolute temperature, b_L is the Langmuir constant. The ΔH^0 , and ΔS^0 values are obtained from the slope and intercept of the plot of $\ln b_L$ vs 1/T (Fig. 4).

Table S4 summarizes the thermodynamic parameters. The endothermic nature is confirmed by ΔH^0 's positive sign and the reaction is more favorable at higher temperatures. Since, the ΔH^0 values are less than 40 kJ/mol, suggesting that there are physical forces existing in MB sorption process. The positive ΔS^0 value showed that the interaction between MB and ZMS/MS would enhance entropy, resulting in more degrees of freedom for solute molecules (Abd El-Magied et al. 2017). The negative ΔG^0 values (in the same range from -32.71 to -39.13 kJ mol⁻¹); imply that the sorption process is spontaneous. The absolute ΔG^0 values is proportional with the temperature. Moreover, Table S4 indicates that the reaction is

controlled by entropic changes than by enthalpy changes ($|\Delta H^\circ| < |T\Delta S^\circ|$) (with values very close).

Photodegradation of MB over prepared catalyst

For catalytic application, the low concentrations of MB dye were used. According to Elaziouti et al. (2011), higher concentrations in catalytic reactions can block or coat the catalyst surface, which reduces the catalyst's catalytic efficiency by absorbing a significant amount of light by the dye molecules rather than the catalyst particles, reducing light penetration to the catalyst's surface, and shielding the light (Saggiaro et al. 2011). Moreover, it inhibits the reaction of adsorbed dye molecules with the photo-induced positive holes or reactive oxygen species (ROS), since there is no direct contact of the semiconductor with them (Akpan and Hameed 2009).

Verma et al. (Verma et al. 2019), studied the effect of initial dye concentration low and high concentrations (5–75 $\mu\text{g/L}$), and he deduced that, the dye concentration (MB) decreased exponentially with time particularly at low initial concentrations of the dye and the apparent rate constant was obtained from single exponential decay. The exponential decay of the dye concentration with light irradiation time shows first order rate kinetics of the associated dye degradation process. Such results have also been reported for other photocatalytic systems (Atitar et al. 2018). So, this study was conducted at low concentrations.

The adsorbed dye molecules undergo several chemical reactions (N-demethylation, deamination, and oxidative processes) caused by photogenerated charge carriers and reactive oxygen radicals in the observed heterogeneous photocatalytic dye degradation. Figure 5 plots the photodegradation of MB+ against the exposure time.; the reaction rate of both catalysts increased with increasing the reaction time. After 45 minutes, the MS and ZMS catalysts degraded the MB by 72.4% and 100%, respectively. The presence of ZS in the ZMSnanocomposite increased the rate of electron and hole pairs separation, as well as the enhanced the surface area (Li et al. 2018). As a result, MS acts as a photosensitizer enhancing ZS photocatalytic activity (Krishnan et al. 2019; Li et al. 2018). The synergistic effect of two semiconductors (ZnS and MoS_2) could explain the improved photocatalytic activity (Cheng et al. 2017; Lin et al. 2015; Zhang et al. 2020a). Also, the ZMS composite possesses a special interface and nanostructure that increases the visible light absorption and increases the electron-hole pair separation.

The kinetics of the photodegradation of MB catalyzed by both as-synthesized catalysts are subjected to the pseudo-first-order (i.e. the dye absorbance decreased exponentially with time (Harish et al. 2019, Verma et al. 2019)) and can be written as $\ln[C_t/C_0] = -kt$, where k is the rate constant (obtained from the slope of the above linear relation), and C_t and C_0 are the MB

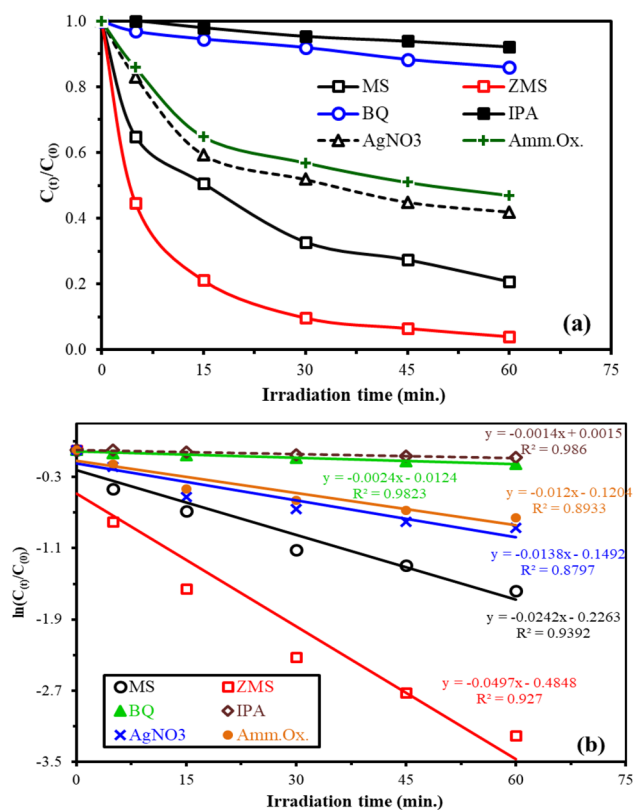


Fig. 5 The photodegradation of MB dye (C_0 : 13–17 mg/L) with irradiation time (a) using tungsten halogen lamp in presence of MS and ZMS nanocomposite (0.5 g/L) and different scavengers agents (10 mmol/100mL MB), and Pseudo-first-order linear relation of $\ln(C_t/C_0)$ vs the irradiation time (b)

concentration at times t and 0 min, respectively (Verma et al. 2019). $\ln(C_t/C_0)$ plotted against irradiation time t (Fig. 5).

A linear relationship exists for the entire reaction course. The apparent rate constants (k) values (Fig. 5) for MB discoloration were 0.024 and 0.0488 min^{-1} , using MS and ZMS, respectively. The higher k (rate constant) for ZMS nanocomposites was nearly three times higher than for pure MS (Sabarinathan et al. 2017); implying that ZMS possess more efficient photocatalytic ability for MB degradation (i.e. the band capacity of MS and ZS is matching). The conductive band and valence band edge positions of MS are consistent with those of ZS, making electrons and holes transport to MS easier. So, the transfer of holes to MS increases the separation of charges resulting in acting the MS as a site of oxidation. Therefore, both MS and ZS semiconductors have conductive band potentials, which prevent electrons and holes in the composite from recombining (Morshedy et al. 2021; Vattikuti et al. 2016). These results reveal the superior catalytic activity of ZMS nanocomposite towards MB degradation. This is due to, the MSnanosheets network decorated by ZS nanoparticles, which connects two inexpensive, versatile, and chemically stable semiconductor materials (Krishnan et al. 2019; Lin et al. 2015; Vattikuti et al. 2016). Where, in the case

of ZMS nanocomposites, ZS acts as an n-type semiconductor that has a large band gap (3.6 eV) and MS nanosheets act as a p-type semiconductor with a narrow band gap (1.86 eV) (Li et al. 2018; Lin et al. 2015; Zhang et al. 2020a); as MS resulted in charge separation by lowering the electron and hole pairs recombination rate (Hu et al. 2018; Li et al. 2018).

Table 1 compiles the efficiency and comparison of ZMS with other photocatalysts under different experimental conditions; this makes difficult the effective comparison of the MB degradation when exposed to visible light in terms of the rate constant respective catalytic performances. The rate constant value of MS is comparable with the other catalysts. The superiority of the ZMS for MB degradation is evident from the rate constant comparison (Table 1).

Total organic compounds (TOC) test

The TOC reflects the mineralization of organic matter by measuring the quantity of total organic compounds in the standard solution before and after the photocatalytic reaction converts the organic dye to simpler molecules like CO₂ and H₂O. So, to confirm the rate of MB dye degradation, TOC values were employed. According to the results, MB degrades at a rapid rate using MS/ZMS catalysts. Photocatalytic performances of MS/ZMS catalysts were investigated at different interval times under visible light. As illustrated in Fig. 6, MB mineralization is rapid in the first 30 min. and the greatest TOC reduction was achieved at 45 min.: total mineralization ≈ 70% and 100% TOC removal for the MS and ZMS, respectively.

Scavenger effect and photodegradation mechanism

The generation of reactive oxygen species (ROS) is driven by the capture of photogenerated electrons or holes by various species in the solution, such as dissolved oxygen, hydroxyl ions, and water molecules. The important ROS are hydroxyl radicals ($\bullet\text{OH}$), superoxide radicals ($\bullet\text{O}_2$), holes (h^+_{VB}), and electrons (e^-_{CB}). The influence of active-species scavengers on the photodegradation of MB has been examined and the results are provided in order to study the

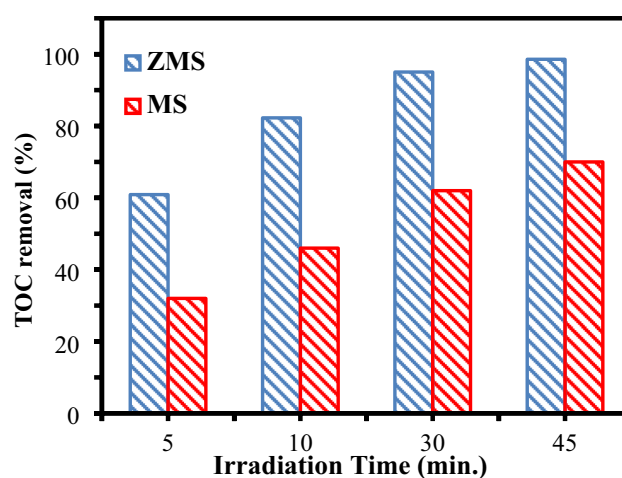


Fig. 6 TOC removal during the photocatalytic treatment of MB using MS and ZMS catalyst

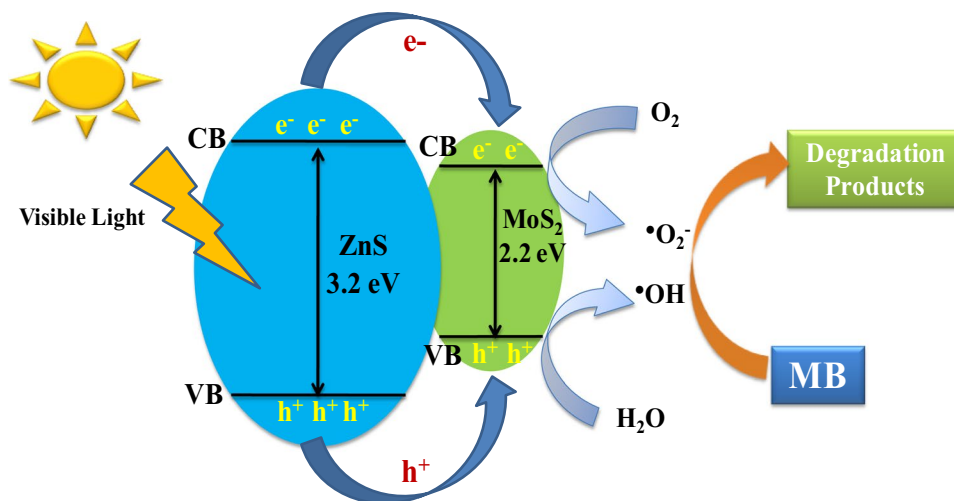
photocatalytic mechanism and identify the primary oxidative species (h^+_{VB} , e^-_{CB} , $\bullet\text{O}_2^-$ and $\bullet\text{OH}$) in the photocatalytic process with increasing time (Fig. 7). Isopropyl alcohol (IPA), benzoquinone (BQ), ammonium oxalate AO ((NH₄)₂C₂O₄), and silver nitrate (AgNO₃) was used to scavenge hydroxyl radicals, superoxide radicals, holes, and electrons. The apparent dye degradation rate constant was discovered to be around 4.99×10^{-2} and 2.4×10^{-2} , for ZMS and pristine MS, respectively. Scavengers had a great impact on reaction rate constants as follow: 1.38×10^{-2} , 1.2×10^{-2} , 2.4×10^{-2} and $1.4 \times 10^{-3} \text{ min}^{-1}$ for AgNO₃, AO, BQ, and IPA agents, respectively (Fig. 5). Moreover, the dye degradation efficiency (removal efficiency, %) has been reduced from 98% (modified catalyst: ZMS) and 79% (pristine MS) to about 58%, 53%, 14 and 8% in the presence of AgNO₃, AO, BQ, and IPA respectively.

The degradation efficiencies drop drastically when IPA and BQ are introduced. Demonstrating that the photocatalytic degradation of MB over the ZMS catalyst is significantly affected by the addition of IPA and BQ rather than AgNO₃ and AO event (Liao et al. 2019), implying that $\bullet\text{OH}$ and $\bullet\text{O}_2$ radicals are the main reactive oxygen species

Table 1 Maximum degradation efficiency for MB with selected catalysts

| Material | Light source | Rate constant (min. ⁻¹) | Cat. Dose, g/L | C ₀ [MB], mg/L | Time (min) | Ref. |
|------------------------------------|---------------------------------|-------------------------------------|----------------|---------------------------|------------|----------------------------|
| MoS ₂ /TiO ₂ | Day lamp (30 W) | ---- | 1.0 | 10.0 | 90 | (Hu et al. 2011) |
| TiO ₂ /zeolite | UV-light (125W) | 0.04694 | 33.3 | 50.0 | 60 | (Liao et al. 2019) |
| MoS ₂ /ZnO | Xe lamp (400W) | 0.01579 | 0.5 | 3.2 | 180 | (Chang et al. 2021) |
| MoS ₂ /TiO ₂ | Asahi spectra (Xe-lamp) (400 W) | 0.4162 | 0.5 | 50.0 | 12 | (Sabarinathan et al. 2017) |
| ZnS/MoS ₂ | Halogen lamp (500 W) | 0.003.61 | 0.17 | 10.0 | 6 h | (Soltani et al. 2012) |
| ZnO/AC-fiber | UV lamp (6W) | 0.042- 0.017 | 1.0 | 50 | 120 | (Albiss et al. 2021) |
| MS | Tungsten halogen lamp (50W) | 0.0242 | 0.5 | 13.2 | 45 | Here |
| ZMS | | 0.0497 | 0.5 | 10.0 | | |

Fig. 7 the proposed mechanism for the photo-degradation process over ZMS catalyst



in charge for the degradation process, while the h^+ and e^- are only partially involved in the photocatalytic process. The radicals ($\bullet OH$) and ($\bullet O_2^-$) react with MB molecules to convert them to harmless forms or fully breakdown them into CO_2 and H_2O (Albiss and Abu-Dalo 2021). Obviously, e^-_{CB} reduces silver ion to metallic Ag ($Ag^+ + e^-_{CB} \rightarrow Ag(s)$), as an effective electron scavenger (El-Morsi et al. 2000), that can act to help in the catalytic degradation. All in all, the degradation mechanisms include all these reactive species (h^+_{VB} , e^-_{CB} , $\bullet O_2^-$ and $\bullet OH$), but mostly it depends on the $\bullet O_2^-$ and $\bullet OH$ species, and has the following sequence: IPA (for $\bullet OH$) > BQ (for $\bullet O_2^-$) > AO (for h^+) > $AgNO_3$ (for e^-_{CB}).

Photocatalytic degradation mechanism (Oxidation Reaction)

To study the photocatalytic mechanism of ZMS nanocomposite, it is necessary to study the electron scavengers' effect. Electron scavengers proved that photocatalytic MB degradation was an oxidative reaction. If the substrate's rate of degradation was being reduced by a reaction with conduction band electrons, e^-_{CB} scavengers would inhibit it down. If the MB substrate was being oxidized, electron scavengers might speed up photocatalytic degradation by reducing the rate of e^-_{CB} and h^+_{VB} (El-Morsi et al. 2000; Mohibbul et al. 2012).

Photoexcitation of semiconductors can result in the formation of electron-donor (reducing) and electron-acceptor (oxidizing) sites, providing great scope for redox reactions. When the semiconductor is irradiated with light ($h\nu$) of greater energy than that of the band gap, an electron is transferred from the valence band (VB) to the conduction band (CB) resulting in a positive hole in the valence band and an electron in the conduction band illustrated in Fig. 7.

The electrons in MS and ZS's valence band (VB) are photoexcited to the conducting band (CB) as free electrons when they are exposed to light, leaving holes in the valence band. Photoinduced electrons (e^-) travel from MS's CB to ZnS's CB, while holes migrate from ZnS's VB to MS's VB. At the same time, the photogenerated holes and electrons migrate to the surface of the catalyst and react with either water (H_2O) or hydroxyl ions (OH^-) adsorbed on the surface of the catalyst to produce hydroxyl $\bullet OH$ and superoxide anion ($\bullet O_2^-$) radicals to degrade the organic pollutants (Hu et al. 2011).

Equations 9–11 can be used to represent the proposed mechanism;

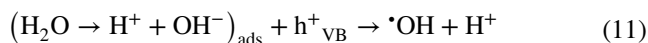
- ZS absorbs photons with high efficiency ($h\nu \geq E_{gap}$):



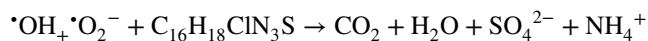
Molecular oxygen is a well-known e^-_{CB} scavenger, and it is transformed to the superoxide anion ($\bullet O_2^-$), which regenerates adsorbed oxygen, O_2 ads.



Neutralization of OH^- group into OH by the hole



The hydroxyl radical ($\bullet OH$) and superoxide radical anions ($\bullet O_2^-$) have been proposed as the principal oxidizing species in photocatalytic oxidation processes based on the scavenger effect results. Organic pollutants will be degraded as a result of these oxidative reactions. The total mineralization of methylene blue ($C_{16}H_{18}ClN_3S$) may be represented by the following equation (Hu et al. 2011).



Conclusion

A simple solvothermal method had been used to prepare pristine MS and ZMS nanocomposite, suitably to be used as photocatalysts for photodegradation of MB. Moreover, the prepared MS and ZMS could be regarded as potential adsorbents to removal of MB from aqueous solutions efficiently. The sorption characteristics for MB sorption were thoroughly examined and compared. The uptake kinetics (equilibrium reached $\sim 25/30$ min) is almost equally fitted by the pseudo-second-order rate equation. The Langmuir model suits the sorption process well with maximum sorption capacities for ZMS ($219.3 \text{ mg MB g}^{-1}$) > MS ($185.5 \text{ mg MB g}^{-1}$): enables single-layer chemical reactions. Thermodynamic parameters (ΔG° , ΔH° and ΔS°) indicate the spontaneous, endothermic nature and randomness increases during the sorption process. Here, the introduction of ZS to MS increased the photocatalytic activity when exposed to visible light. ZMS has superior photocatalytic activity to MS. XRD, HRTEM, XPS, Raman, N_2 adsorption-desorption, EDX, UV-Vis., PL, and zeta potential were all used to investigate the properties of MS and ZMS. Under ideal catalyst dose of 0.5 g/L and neutral pH, the ZMS catalyst displayed the best photodegradation for MB, with an elimination efficiency of about 100% within 45 minutes, compared to 72.4% for MS during the same period light illumination with TOC removal of 98.6 and 70.2%, respectively. Under optimal conditions, TOC analysis was used to determine the mineralization of the model pollutant. The scavenging activity of free radicals revealed the mechanism of the photocatalytic process. We conclude that the ZMS nanocomposite can be utilized as a suitable bifunctional material for future photocatalytic degradation applications based on our thorough investigation of our results.

Supplementary Information The online version contains supplementary material available at <https://doi.org/10.1007/s11356-022-21255-1>.

Acknowledgements The authors acknowledge the support and funding of Research Center for Advanced Material Science (RCAMS) at King Khalid University through Grant No. RCAMS/KKU/007-21.

Author contribution Samira M. Abdel-Azim and Mohammed M. Younus: Conceptualization, Methodology, Investigation, Writing original draft. Mehboobali Pannipara: Conceptualization, Validation. S. Wageh: Methodology, Validation, Resources. Abdelghaffar S. Dhmees and Ahmed A. Galhoum: Conceptualization, Methodology, Resources, Writing—original draft, Writing—review & editing, Supervision.

Data availability All data included in this article are originally generated or analyzed during this study.

Declarations

Ethics approval and consent to participate Not applicable.

Consent for publication Not applicable

Competing interests The authors declare no competing interests.

References

- Abd El-Magied MO, Galhoum AA, Atia AA, Tolba AA, Maize MS, Vincent T, Guibal E (2017) Cellulose and chitosan derivatives for enhanced sorption of erbium (III). *Colloids Surf A Physicochem Eng Asp* 529:580–593
- Akpan UG, Hameed BH (2009) Parameters affecting the photocatalytic degradation of dyes using TiO_2 -based photocatalysts: a review. *J Hazard Mater* 170:520–529
- Albiss B, Abu-Dalo M (2021) Photocatalytic degradation of methylene blue using zinc oxide nanorods grown on activated carbon fibers. *Sustainability* 13:4729. <https://doi.org/10.3390/su13094729>
- Amdeha E, Mohamed RS, Dhmees AS (2021) Sonochemical assisted preparation of ZnS–ZnO/MCM-41 based on blast furnace slag and electric arc furnace dust for Cr (VI) photoreduction. *Ceram Int* 47:23014–23027
- Ashoka S, Nagaraju G, Tharamani CN, Chandrappa GT (2009) Ethylene glycol assisted hydrothermal synthesis of flower like ZnO architectures. *Mater Lett* 63:873–876
- Atitar MF, Bouziani A, Dillert R, El Azzouzi M, Bahnemann DW (2018) Photocatalytic degradation of the herbicide imazapyr: do the initial degradation rates correlate with the adsorption kinetics and isotherms? *Catal Sci Technol* 8:985–995
- Auer G, Woditsch P, Westerhaus A, Kischkewitz J, Griebler WS, Rohe M, Liedekerke MJ (2000) Pigments, inorganic. *White Pigments* 2:1–36
- Azad UP, Ganesan V, Pal M (2011) Catalytic reduction of organic dyes at gold nanoparticles impregnated silica materials: influence of functional groups and surfactants. *J Nanopart Res* 13:3951–3959
- Chang K, Hai X, Pang H, Zhang H, Shi L, Liu G, Liu H, Zhao G, Li M, Ye J (2016) Targeted synthesis of 2H- and 1T-phase MoS_2 monolayers for catalytic hydrogen evolution. *Adv Mater* 28:10033–10041
- Chang Y-C, Lin Y-W, Lu M-Y (2021) Construction of MoS_2/ZnO heterostructures as highly efficient photocatalysts for enhanced visible-light decomposition of methylene blue and hydrogen evolution. *Mater Chem Phys* 266:124560
- Cheng Y, Jin C, Gao F, Wu X, Zhong W, Li S, Chu PK (2009) Raman scattering study of zinc blende and wurtzite ZnS. *J Appl Phys* 106:123505
- Cheng J, Han L, Wei Y, Chen Q (2017) Enhancement of photocatalytic property on ZnS/MoS₂ composite under visible light irradiation. *MATEC Web of Conferences* 108:01008. <https://doi.org/10.1051/mateconf/201710801008>
- Cheng X, Wang L, Xie L, Sun C, Zhao W, Liu X, Zhuang Z, Liu S, Zhao Q (2022) Defect-driven selective oxidation of MoS_2 nanosheets with photothermal effect for Photo-Catalytic hydrogen evolution reaction. *Chem Eng J* 439:135757
- Cheung WH, Szeto YS, McKay G (2007) Intraparticle diffusion processes during acid dye adsorption onto chitosan. *Bioresour Technol* 98:2897–2904
- Dhmees AS, Rashad AM, Eliwa AA, Zawrah M (2019) Preparation and characterization of nano $\text{SiO}_2@ \text{CeO}_2$ extracted from blast furnace slag and uranium extraction waste for wastewater treatment. *Ceram Int* 45:7309–7317
- Ding Y, Guo X, Du B, Hu X, Yang X, He Y, Zhou Y, Zang Z (2021) Low-operating temperature ammonia sensor based on Cu_2O nanoparticles decorated with p-type MoS_2 nanosheets. *J Mater Chem C* 9:4838–4846
- Doğan M, Özdemir Y, Alkan M (2007) Adsorption kinetics and mechanism of cationic methyl violet and methylene blue dyes onto sepiolite. *Dyes Pigments* 75:701–713

- Ebrahimi A, Jafari N, Ebrahimpour K, Karimi M, Rostamnia S, Behnami A, Ghanbari R, Mohammadi A, Rahimi B, Abdolhnejad A (2021) A novel ternary heterogeneous $\text{TiO}_2/\text{BiVO}_4/\text{NaY-Zeolite}$ nanocomposite for photocatalytic degradation of microcystin-leucine arginine (MC-LR) under visible light. *Ecotoxicol Environ Saf* 210:111862
- El Sharkawy HM, Dhmees AS, Tamman A, El Sabagh S, Aboushahba R, Allam NK (2020) N-doped carbon quantum dots boost the electrochemical supercapacitive performance and cyclic stability of MoS_2 . *J Energy Storage* 27:101078
- Elaziouti A, Laouedj N, Ahmed B (2011) ZnO-assisted photocatalytic degradation of congo Red and benzopurpurine 4B in aqueous solution. *J Chem Eng Process Technol* 2:1–9. <https://doi.org/10.4172/2157-7048.1000106>
- Elkholy AE, Dhmees AS, Heikal FE-T, Deyab M (2019) Mesoporous ZnMoS_4 as a supercapacitor electrode material with battery-like behavior. *New J Chem* 43:1987–1992
- El-Morsi TM, Budakowski WR, Abd-El-Aziz AS, Friesen KJ (2000) Photocatalytic Degradation of 1,10-Dichlorodecane in Aqueous Suspensions of TiO_2 : A Reaction of Adsorbed Chlorinated Alkane with Surface Hydroxyl Radicals. *Environ Sci Technol* 34:1018–1022
- Galhoun AA (2019) Facile synthesis of functionalized polyglycidyl methacrylate-magnetic nanocomposites for enhanced uranium sorption. *RSC Adv* 9:38783–38796
- Gao M-R, Liang J-X, Zheng Y-R, Xu Y-F, Jiang J, Gao Q, Li J, Yu S-H (2015) An efficient molybdenum disulfide/cobalt diselenide hybrid catalyst for electrochemical hydrogen generation. *Nat Commun* 6:5982–5982
- Gao H, Wang S, Fang L, Sun G, Chen X, Tang S, Yang H, Sun G, Li D (2021) Nanostructured spinel-type M (M= Mg, Co, Zn) Cr_2O_4 oxides: novel adsorbents for aqueous Congo red removal. *Mater Today Chem* 22:100593
- Geng X, Jiao Y, Han Y, Mukhopadhyay A, Yang L, Zhu H (2017) Free-standing Metallic 1T MoS_2 with Dual Ion Diffusion Paths as High Rate Anode for Sodium-Ion Batteries. *Adv Funct Mater* 27:1702998
- Gopalakrishnan A, Singh SP, Badhulika S (2020) Reusable, few-layered- MoS_2 nanosheets/graphene hybrid on cellulose paper for superior adsorption of methylene blue dye. *New J Chem* 44:5489–5500
- Harish S, Prachi AJ, Navaneethan M, Shimomura M, Ikeda H, Hayakawa Y (2019) Synergistic interaction of 2D layered MoS_2/ZnS nanocomposite for highly efficient photocatalytic activity under visible light irradiation. *Appl Surf Sci* 488:36–45
- Hayati P, Mehrabadi Z, Karimi M, Janczak J, Mohammadi K, Mahmoudi G, Dadi F, Fard MJS, Hasanzadeh A, Rostamnia S (2021) Photocatalytic activity of new nanostructures of an Ag(I) metal-organic framework (Ag-MOF) for the efficient degradation of MCPA and 2, 4-D herbicides under sunlight irradiation. *New J Chem* 45:3408–3417
- He Y, Wang D, Li X, Fu Q, Yin L, Yang Q, Chen H (2021) Photocatalytic degradation of tetracycline by metal-organic frameworks modified with Bi_2WO_6 nanosheet under direct sunlight. *Chemosphere* 284:131386
- Hou X, Mensah A, Zhao M, Cai Y, Wei Q (2020) Facile controlled synthesis of monodispersed $\text{MoO}_3\text{-MoS}_2$ hybrid nanospheres for efficient hydrogen evolution reaction. *Appl Surf Sci* 529:147115
- Hu KH, Cai YK, Li S (2011) Photocatalytic Degradation of Methylene Blue on $\text{MoS}_2/\text{TiO}_2$ Nanocomposite. *Adv Mater Res* 197-198:996–999
- Hu X, Deng F, Huang W, Zeng G, Luo X, Dionysiou DD (2018) The band structure control of visible-light-driven $\text{rGO}/\text{ZnS-MoS}_2$ for excellent photocatalytic degradation performance and long-term stability. *Chem Eng J* 350:248–256
- Hu X, Chen C, Zhang D, Xue Y (2021) Kinetics, isotherm and chemical speciation analysis of Hg (II) adsorption over oxygen-containing MXene adsorbent. *Chemosphere* 278:130206
- Ibrahim MM, El-Sheshtawy HS, Abd El-Magied MO, Dhmees AS (2021) Mesoporous Al_2O_3 derived from blast furnace slag as a cost-effective adsorbent for U(VI) removal from aqueous solutions. *Int J Environ Anal Chem* <https://doi.org/10.1080/03067319.2021.1900150>
- Issaabadi Z, Nasrollahzadeh M, Sajadi SM (2017) Green synthesis of the copper nanoparticles supported on bentonite and investigation of its catalytic activity. *J Clean Prod* 142:3584–3591
- Krishnan U, Kaur M, Kaur G, Singh K, Dogra AR, Kumar M, Kumar A (2019) MoS_2/ZnO nanocomposites for efficient photocatalytic degradation of industrial pollutants. *Mater Res Bull* 111:212–221
- Kumar A, Chandel M, Sharma A, Thakur M, Kumar A, Pathania D, Singh L (2021) Robust visible light active $\text{PANI}/\text{LaFeO}_3/\text{CoFe}_2\text{O}_4$ ternary heterojunction for the photo-degradation and mineralization of pharmaceutical effluent: Clozapine. *J Environ Chem Eng* 9:106159
- Li Z, Meng X, Zhang Z (2018) Recent development on MoS_2 -based photocatalysis: A review. *J Photochem Photobiol C: Photochem Rev* 35:39–55
- Liao G, He W, He Y (2019) Investigation of Microstructure and Photocatalytic Performance of a Modified Zeolite Supported Nanocrystal TiO_2 Composite. *Catalysts* 9:502
- Lin M-H, Ho C-H (2017) Synthesis and Optical Characterization of Oxygen-Incorporated $\text{ZnS}_{(1-x)}\text{O}_x$ for UV-Visible Color Palette Light-Emission Matter. *ACS Omega* 2:4514–4523
- Lin T, Wang J, Guo L, Fu F (2015) $\text{Fe}_3\text{O}_4@/\text{MoS}_2$ Core-Shell Composites: Preparation, Characterization, and Catalytic Application. *J Phys Chem C* 119:13658–13664
- Lin Y, Ren P, Wei C (2019) Fabrication of $\text{MoS}_2/\text{TiO}_2$ heterostructures with enhanced photocatalytic activity. *Cryst Eng Comm* 21:3439–3450
- Liu L, Huang Y, Zhang S, Gong Y, Su Y, Cao J, Hu H (2019) Adsorption characteristics and mechanism of Pb(II) by agricultural waste-derived biochars produced from a pilot-scale pyrolysis system. *Waste Manag* 100:287–295
- Liu X, Wang Y, Yang Y, Lv W, Lian G, Golberg D, Wang X, Zhao X, Ding Y (2020a) A $\text{MoS}_2/\text{Carbon}$ hybrid anode for high-performance Li-ion batteries at low temperature. *Nano Energy* 70:104550
- Liu X, Zhang X, Ma S, Tong S, Han X, Wang H (2020b) Flexible amorphous MoS_2 nanoflakes/N-doped carbon microtubes/reduced graphite oxide composite paper as binder free anode for full cell lithium ion batteries. *Electrochim Acta* 333:135568
- Lydia Caroline M, Vasudevan S (2009) Growth and characterization of pure and doped bis thiourea zinc acetate: Semiorganic nonlinear optical single crystals. *Curr Appl Phys* 9:1054–1061
- Mahmoodi NM, Arami M, Limae NY, Tabrizi NS (2006) Kinetics of heterogeneous photocatalytic degradation of reactive dyes in an immobilized TiO_2 photocatalytic reactor. *J Colloid Interface Sci* 295:159–164
- Mao M, Jiang L, Wu L, Zhang M, Wang T (2015) The structure control of $\text{ZnS}/\text{graphene}$ composites and their excellent properties for lithium-ion batteries. *J Mater Chem A* 3:13384–13389
- Mohibbul M, Bahnemann D, Muneer M (2012): Photocatalytic Degradation of Organic Pollutants: Mechanisms and Kinetics, Organic Pollutants Ten Years After the Stockholm Convention - Environmental and Analytical Update
- Morshedy AS, Tawfik SM, Hashem KM, Abd El-Aty DM, Galhoun AA, Mostafa MS, Guibal E (2021) The production of clean diesel fuel by facile sun light photocatalytic desulfurization process using Cd-based diacetate as a novel liquid photocatalyst. *J Clean Prod* 279:123629
- Neiber RR, Galhoun AA, El Sayed IE-T, Guibal E, Xin J, Lu X (2022) Selective lead (II) sorption using aminophosphonate-based sorbents: Effect of amine linker, characterization and sorption performance. *Chem Eng J* 442:136300
- Nezamzadeh-Ejhih A, Banan Z (2011) A comparison between the efficiency of CdS nanoparticles/zeolite A and CdO/zeolite A as

- catalysts in photodecolorization of crystal violet. *Desalination* 279:146–151
- Pathania D, Sharma A, Kumar S, Srivastava AK, Kumar A, Singh L (2021) Bio-synthesized Cu–ZnO hetero-nanostructure for catalytic degradation of organophosphate chlorpyrifos under solar illumination. *Chemosphere* 277:130315
- Rao Akshatha S, Sreenivasa S, Parashuram L, Raghu MS, Yogesh Kumar K, Madhu Chakrapani Rao T (2020) Visible-Light-Induced Photochemical Hydrogen Evolution and Degradation of Crystal Violet Dye by Interwoven Layered MoS₂/Wurtzite ZnS Heterostructure Photocatalyst. *ChemistrySelect* 5:6918–6926
- Rashad MM, El-Sayed IE, Galhoum AA, Abdeen MM, Mira HI, Elshehy EA, Zhang S, Lu X, Xin J, Guibal E (2021) Synthesis of α -aminophosphonate based sorbents Influence of inserted groups (carboxylic vs. amine) on uranyl sorption. *Chem Eng J* 421:127830
- Sabarinathan M, Harish S, Archana J, Navaneethan M, Ikeda H, Hayakawa Y (2017) Highly efficient visible-light photocatalytic activity of MoS₂-TiO₂ mixtures hybrid photocatalyst and functional properties. *RSC Adv* 7:24754–24763
- Saggiaro EM, Oliveira AS, Pavesi T, Maia CG, Ferreira LFV, Moreira JC (2011) Use of titanium dioxide photocatalysis on the remediation of model textile wastewaters containing azo dyes. *Molecules* 16:10370–10386
- Shen K, Cui Y, Zhang D, Liu M, Huang H, Sha X, Deng F, Zhou N, Zhang X, Wei Y (2020) Biomimetic preparation of MoS₂-Fe₃O₄ MNPs as heterogeneous catalysts for the degradation of methylene blue. *J Environ Chem Eng* 8:104125
- Soltani N, Saion E, Hussein MZ, Erfani M, Abedini A, Bahmanrokh G, Navasery M, Vaziri P (2012) Visible light-induced degradation of methylene blue in the presence of photocatalytic ZnS and CdS nanoparticles. *Int J Mol Sci* 13:12242–12258
- Tien C (1994) Adsorption Calculations and Modeling. Butterworth-Heinemann Series in Chemical Engineering, Butterworth-Heinemann, p 243
- Tolba AA, Mohamady SI, Hussin SS, Akashi T, Sakai Y, Galhoum AA, Guibal E (2017) Synthesis and characterization of poly(carboxymethyl)-cellulose for enhanced La(III) sorption. *Carbohydr Polym* 157:1809–1820
- Uddin MJ, Ampiauw RE, Lee W (2021) Adsorptive removal of dyes from wastewater using a metal-organic framework: A review. *Chemosphere* 284:131314
- Vattikuti SVP, Byon C, Jeon S (2016) Enhanced photocatalytic activity of ZnS nanoparticles loaded with MoS₂ nanoflakes by self-assembly approach. *Phys B Condens Matter* 502:103–112
- Verma S, Rao BT, Jayabalan J, Rai S, Phase D, Srivastava A, Kaul R (2019) Studies on growth of Au cube-ZnO core-shell nanoparticles for photocatalytic degradation of methylene blue and methyl orange dyes in aqueous media and in presence of different scavengers. *J Environ Chem Eng* 7:103209
- Wahab R, Ansari SG, Kim Y-S, Dhage MS, Seo HK, Song M, Shin H-S (2009) Effect of annealing on the conversion of ZnS to ZnO nanoparticles synthesized by the sol-gel method using zinc acetate and thiourea. *Met Mater Int* 15:453
- Waheed A, Baig N, Ullah N, Falath W (2021) Removal of hazardous dyes, toxic metal ions and organic pollutants from wastewater by using porous hyper-cross-linked polymeric materials: A review of recent advances. *J Environ Manag* 287:112360
- Wang S, Li G, Du G, Jiang X, Feng C, Guo Z, Kim S-J (2010) Hydrothermal Synthesis of Molybdenum Disulfide for Lithium Ion Battery Applications. *Chin J Chem Eng* 18:910–913
- Wang Z, Zhang J, Wen T, Liu X, Wang Y, Yang H, Sun J, Feng J, Dong S, Sun J (2020) Highly effective remediation of Pb (II) and Hg (II) contaminated wastewater and soil by flower-like magnetic MoS₂ nanohybrid. *Sci Total Environ* 699:134341
- Yu Y, Bataller AW, Younts R, Yu Y, Li G, Puzetzy AA, Geoghegan DB, Gundogdu K, Cao L (2019) Room-temperature electron-hole liquid in monolayer MoS₂. *ACS Nano* 13:10351–10358
- Zamiri R, Tobaldi DM, Ahangar HA, Rebelo A, Seabra MP, Belsley MS, Ferreira J (2014) Study of far infrared optical properties and photocatalytic activity of ZnO/ZnS hetero-nanocomposite structure. *RSC Adv* 4:35383–35389
- Zhang K, Meng W, Wang S, Mi H, Sun L, Tao K (2020a) One-step synthesis of ZnS@MoS₂ core-shell nanostructure for high efficiency photocatalytic degradation of tetracycline. *New J Chem* 44:472–477
- Zhang L, He X, Zhou Q, Hu X (2020b) Fabrication of 1T-MoS₂ nanosheets and the high-efficiency removal of toxic metals in aquatic systems: Performance and mechanisms. *Chem Eng J* 386:123996
- Zhang Y, Kuwahara Y, Mori K, Louis C, Yamashita H (2020c) Hybrid phase 1T/2H-MoS₂ with controllable 1T concentration and its promoted hydrogen evolution reaction. *Nanoscale* 12:11908–11915
- Zhao Y-F, Yang Z-Y, Zhang Y-X, Jing L, Guo X, Ke Z, Hu P, Wang G, Yan Y-M, Sun K-N (2014) Cu₂O Decorated with Cocatalyst MoS₂ for Solar Hydrogen Production with Enhanced Efficiency under Visible Light. *J Phys Chem C* 118:14238–14245
- Zhao H, Liu W, Zhu J, Shen X, Xiong L, Li Y, Li X, Liu J, Wang R, Jin C, Yu R (2015) Structural transition behavior of ZnS nanotetrapods under high pressure. *High Pressure Res* 35:9–15
- Zheng Y, Wang J, Wang Y, Zhou H, Pu Z, Yang Q, Huang W (2019) The Combination of MoS₂/WO₃ and Its Adsorption Properties of Methylene Blue at Low Temperatures. *Molecules* 25:2

Publisher's note Springer Nature remains neutral with regard to jurisdictional claims in published maps and institutional affiliations.